



ASME Accepted Manuscript Repository

Institutional Repository Cover Sheet

First

Last

Numerical Simulation of Airborne Salt Particle Behavior in Dry Gauze Method Using Porous Medi
ASME Paper Title: Model

Authors: Yuta Tsubokura, Kyohei Noguchi, Tomomi Yagi

ASME Journal Title: Journal of Applied Mechanics

Volume/Issue Volume 88 / Issue 10 Date of Publication (VOR* Online) May 24, 2021

ASME Digital Collection URL: <https://asmedigitalcollection.asme.org/appliedmechanics/article/88/10/101001/1109015/>

DOI: <https://doi.org/10.1115/1.4051114>

*VOR (version of record)

Numerical Simulation of Airborne Salt Particle Behavior in Dry Gauze Method Using Porous Media Model

Yuta Tsubokura¹

Department of Civil and Earth Resources Engineering, Kyoto University
Kyoto daigaku-katsura, Nishikyo-ku, Kyoto 615-8540, Japan
tsubokura.yuuta.73s@st.kyoto-u.ac.jp

Kyohei Noguchi

Department of Civil and Earth Resources Engineering, Kyoto University
Kyoto daigaku-katsura, Nishikyo-ku, Kyoto 615-8540, Japan
noguchi.kyohei.7z@kyoto-u.ac.jp

Tomomi Yagi

Department of Civil and Earth Resources Engineering, Kyoto University
Kyoto daigaku-katsura, Nishikyo-ku, Kyoto 615-8540, Japan
yagi.tomomi.7a@kyoto-u.ac.jp

ABSTRACT

Airborne salt accelerates the corrosion of steel materials and, thus, must be quantitatively evaluated for the management of steel structures. In Japan, the dry gauze method, which uses a gauze embedded in a wooden frame, is often used to evaluate the amount of airborne salt. However, its collection efficiency for salt particles has not been verified owing to the complex airflows around the device. Therefore, as a first step to clarify the collection efficiency, the authors simulated the flow field around the collection device using computational fluid dynamics. In this study, the gauze was modeled as a porous medium to reduce the computational costs. Wind tunnel tests were performed to obtain the pressure loss coefficients of the gauze, which is necessary for the porous media method. Subsequently, particle tracking was performed in the calculated flow field, and the collection efficiency was evaluated under the condition of a filtration efficiency of 100%. The flow fields around the device were accurately reproduced using the porous media model, which considered both the tangential and normal resistances of the gauze. This result suggests that the tangential resistance must be considered in the porous media model when the porosity of an object is small, even if the thickness is small. The dependence of collection efficiency on wind speed and direction was quantitatively evaluated. The results showed that the collection efficiency was greatly affected by the complicated flow field around the device due to the combination of the gauze and wooden frame.

¹ Corresponding author

1 Introduction

Airborne salt accelerates the corrosion of steel materials and, thus, must be quantitatively evaluated for the management of steel structures. According to a survey on the repair of the superstructures of bridges in Japan [1], half of the bridges are damaged owing to the corrosion of steel components, indicating that corrosion is a major factor in structural deterioration. Therefore, when performing steel or concrete structure maintenance, the amount of airborne salt reaching the construction site and the amount of salt adhering to the surface of the structure must be determined. In fact, in Japan, a criterion for using weathering steel without coating is regulated based on the amount of airborne salt in the atmosphere [2].

Thus, many researchers have investigated the airborne salt content and adhesion of airborne salt particles to the surface of the structure. Manders et al. [3] used a chemical transport model to reproduce the distribution of airborne salt concentrations in Europe. Noguchi et al. [4] proposed a method to calculate the amount of salt adhering to each part of a bridge based on airborne sea salt concentration and the flow field around the bridge obtained by computational fluid dynamics (CFD). The Cooperative Research Centre for Construction Innovation (CRCCI) [5] calculated the amount of adhesion to each part of a bridge while changing the release height of the particles to examine the effect of the height of the bridge from the sea level. Zhou et al. [6] found that the chloride deposition on a mortar specimen surface was usually higher than that on a steel surface in a natural exposure experiment.

The methods for observing the amount of airborne salt can be classified into active collecting methods, which require power, and passive collecting methods, which do not require power. The filter-pack method is an active collecting method, in which the airflow is forcibly suctioned and particles are collected by a filter [7]. Passive collecting methods, including the wet candle [8], Doken tank [9], and dry gauze methods, are often used. The dry gauze method (hereinafter referred to as the gauze method) is the most frequently used method to measure airborne salt content in Japan. The gauze method is defined in the Japanese Industrial Standard (JIS) [10]. Figs. 1 (a) and (b) show the collection device of the gauze method, which consists of two sheets of 100 mm-square gauze installed on a wooden frame of 150 mm-square outer size. The collection device of the gauze method is usually installed in an arbitrary location in a steel or concrete structure. This method evaluates the amount of salt captured by the gauze as salty air passes through it. Fig. 1(c) shows an example of a collection device installed under a bridge girder. Occasionally, this device is installed near the surface of a structure to evaluate the local corrosive environment [11]. Because the device is easy to install and measure owing to its simple structure and mechanism, the observation results of the amount of airborne salt at bridge sites obtained by this method are numerous in Japan. However, the collection efficiency of salt particles has not been sufficiently ascertained yet, and whether the true amount of airborne salt particles is usually gauged is still unclear. Obata and Murakami [12] evaluated the collection efficiency of the gauze method by outdoor observations and reported that it is different in each observation period. However, they did not sufficiently explain the cause of this difference.

To be accurate, the following two factors are considered important in the collection efficiency of the gauze method. First, not all the approaching particles necessarily reach the gauze part because

the collection device itself disturbs the approaching flow. Second, after reaching the gauze, some particles slip through the gauze mesh. Thus, the collection efficiency (γ) can be formulated as the product of the arrival rate of particles to the gauze part (α) and the capture rate of salt particles by the gauze fiber (β) as follows:

$$\gamma = \alpha\beta \quad (1)$$

In this study, the arrival rate (α) is defined as the ratio of the number of particles that reach the gauze part to the number of particles that come from upstream in the gauze projected area. Additionally, the capture rate (β) is defined as the ratio of the number of particles captured by gauze fibers to the number of particles that flow into the gauze part. Previous studies on the collection efficiency did not distinguish these two factors, which made a comprehensive discussion difficult. Moreover, the complicated flow field around the device due to the combination of the gauze layer and wooden frame is likely another cause. Therefore, as a first step to realize an appropriate evaluation of the corrosive environment of a structure using the gauze method, this study focused on the arrival rate (α) and investigated its dependency on the wind conditions based on a flow field analysis. The mechanism by which the gauze captures salt particles (β) should be investigated in the future. Therefore, β is set to 1 in this study. Furthermore, the flow field around the collection device was calculated using CFD to discuss the collection efficiency, especially with respect to wind speed and direction. Additionally, we calculated the movement of particles near the collection device in the calculated flow field to investigate the arrival rate.

In a flow field analysis using CFD around the collection device in the gauze method, the reproduction of the resistance caused by the gauze is an impediment. One way to solve this problem

is to accurately or roughly reproduce the structure of an analysis object. Basnet et al. [13] used this method to investigate the characteristics of the flow past a snow fence. Another way is to represent the fluid resistance by incorporating the relationship between the fluid velocity and pressure loss into the equation of motion instead of reproducing the detailed shape of the analysis object. This method is called a porous media model and is often applied to the analysis of the flow through a porous structure [14, 15]. The relationship between the pressure loss and the structure of porous materials has been reported in a number of studies [16-18].

In this study, to represent a fine structure of gauze fiber, a very fine computational grid is required, which is computationally expensive. Therefore, we adopted a method that models the gauze using a porous media model. Wind tunnel tests were performed to obtain the pressure loss coefficients of the gauze. The porous media model can be applied to the gauze because of its homogeneous structure. However, the applicability of the porous media model to extremely thin objects with a small porosity, such as gauze, has not been sufficiently investigated. Additionally, although the porous media model has been employed often, the resistance in the tangential direction has not been discussed sufficiently. Kuroyanagi [19] calculated a flow field around a plastic greenhouse with a two-dimensional porous media model that did not consider the tangential resistance of the porous medium and obtained quantitatively valid results. However, the porosity of the greenhouse they used was much larger than that of the gauze used in this study. Noda et al. [20] also calculated the flow fields around windbreak nets with various porosities using a porous media model that did not consider the tangential resistance. However, even though the wind velocity profiles around nets with relatively large porosities were reproduced well compared with the

experimental results, there was a difference between the numerical and experimental values for nets with relatively small porosities. On the other hand, Mahgoub and Ghani [21] calculated the flow fields around windbreaks using a three-dimensional porous media model in which the tangential resistance was considered. However, the thickness of the windbreak used by them was significantly larger than those of the gauze used in this study. Therefore, this study also discussed the effect of the tangential resistance when applying the porous media model to very thin structures such as gauze.

In the research process, the flow field around the collection device was first evaluated by visualization tests through particle image velocimetry (PIV) analysis. Then, the flow field around the collection device was calculated using CFD and compared with the results of the PIV analysis. Moreover, to validate the flow field obtained by CFD, the wind speed in the vicinity of the collection device and the aerodynamic force coefficients of the device were measured in the wind tunnel tests. They were then compared with the analysis results. Finally, by performing a particle scattering analysis of the flow field around the collection device obtained using CFD, we ascertained the amount of salt particles that reached the gauze part considering wind speed, wind direction, and salt particle size.

2 Wind tunnel tests and flow field analysis method

The collection device used in the wind tunnel tests and CFD was a wooden frame with an outer length of 150 mm, as specified in JIS Z 2382. The thickness of the wooden frame and the porosity of the gauze are not specified in JIS. In this study, a wooden frame with a thickness of 18 mm was

used. According to previous studies on the aerodynamic characteristics of a square plate [22, 23], the aerodynamic force coefficient varies little with the side ratio when the thickness is much smaller than the outer length. Therefore, although there is room for considering the thickness of the device, the effect on the flow field is probably small as the thickness is much smaller than the outer length of the device. A common medical gauze (HAKUJUJI, Absorbent Gauze) with a gauze fiber diameter of 0.2 mm, aperture of 0.7 mm, and porosity of 0.605 was used. According to previous study [24], the aerodynamic characteristics of the net structures vary with the porosity of the structure. However, the purpose of this study was to observe changes in the collection efficiency caused by the wind conditions; thus, only one type of gauze was used. In the future, the effect of the porosity of the gauze on the collection efficiency should be investigated.

In this section, we first explain the wind tunnel tests. Then, we show the flow field analysis method using CFD around the collection device.

2.1 Wind tunnel tests

First, to study the characteristics of the flows and compare them with those from the CFD, the flow field around the collection device was evaluated by flow visualization through PIV analysis. Next, to evaluate the validity of the flow field obtained by CFD, the wind speed in the vicinity and the aerodynamic force coefficients of the collection device were measured in the wind tunnel tests. Finally, the pressure loss coefficients were measured in wind tunnel tests, as this is necessary for the boundary condition of the gauze in CFD. In the following sections, we describe the setup of the wind tunnel tests.

2.1.1 Flow visualization through PIV analysis

An Eiffel-type wind tunnel was used in the visualization test, as shown in Fig. 2. In this study, all the tests, except the pressure loss experiment, were conducted using this wind tunnel under smooth flow conditions. This wind tunnel had a test section of 1,800 mm in height and 1,000 mm in width. It had a uniform wind speed distribution at the installation position of the device. The turbulence intensity in the mainstream direction is 0.3% at a wind speed of 10 m/s, which can be regarded as smooth in accordance with the Honshu–Shikoku Bridge Authority [25]. The collection device was supported by a round bar placed on the wind tunnel floor, as shown in Fig. 2(a). The blockage ratio, which is defined as the ratio of the cross-sectional area of the collection device to that of the wind tunnel, reached 1.25% when the collection device and the approaching wind were orthogonal to each other. The approaching wind speed was set to 1 m/s, and the corresponding Reynolds number ($Re = UD/\nu$, D : outer size of the collection device, ν : kinematic viscosity) was 1.0×10^4 . To consider the wind directions, the device was horizontally rotated. The approaching wind angle was set to 0° , 22.5° , 45° , and 67.5° , where 0° indicates that the approaching wind is orthogonal to the device.

A glycol/water solution was used for the tracer particles, and their sizes were in the 0.3–1 μm range. The tracer particles were supplied by a smoke generator (KANOMAX, Model 8304), and then diffused into the wind tunnel by a wing-type smoke diffuser (Fig. 2(b)) installed 3,000 mm upstream from the collection device. A continuous Nd:YVO₄ laser (KATO KOKEN, PIV Laser LB2000, power: 2 J/s, wavelength: 532 nm) was employed to visualize the central cross-section of the collection device, and a CMOS camera (KATO KOKEN, k8-USB, resolution: 1024×1024

pixels) was installed in the upper part of the wind tunnel to capture the particle images. As shown in Fig. 2(c), in part of the flow field, the laser sheet was blocked by a collection device. For this region, the wind speed was linearly interpolated from the surrounding grid points in the PIV analysis.

The size of the visualized cross-section was $300 \text{ mm} \times 300 \text{ mm}$, and the spatial resolution was $3.4 \times 3.4 \text{ pixels/mm}$. The images were captured at 300 fps for 10 s with a shutter speed of $1/300 \text{ s}$. A total of 3,000 frames were used to calculate the time-averaged wind velocity. In the PIV analysis, the velocity distribution was calculated using the digital image correlation [26], which calculates the displacement of particles between two consecutive images to determine the velocity distribution. The interrogation window size was $32 \times 32 \text{ pixels}$, with a 50% overlap. The error vectors were removed by comparison with the mean of the velocity vectors of the eight surrounding points based on statistical processing [27].

2.1.2 Wind speed measurement

The collection device was installed inside the wind tunnel, as shown in Fig. 3(a). The maximum blockage ratio was 1.25% when the collection device and the approaching wind were orthogonal to each other. The wind speed was measured by a hot-wire anemometer near the collection device (KANOMAX, Anemomaster Professional Standard, Model 6036). This anemometer can measure the time-averaged wind speed in one direction from 0.01 to 30.0 m/s with the tip probe and has an accuracy of $\pm 3\%$ of reading or 0.015 m/s (the largest one is applied). To consider the wind directions, the device was horizontally rotated. The approaching wind angle was set to 0° , 22.5° , 45° , and 67.5° , whereas the approaching wind speed was set to 1, 3, and 5 m/s ($Re = 1.0 \times 10^4$, 3.0×10^4 , and $5.0 \times$

10^4). The 1-min average wind speeds in the main flow direction at nine points on the front and back sides of the gauze (see Fig. 3(b)) were measured. They were 10 mm away from the gauze surface upstream and downstream, respectively.

2.1.3 Aerodynamic force coefficient measurements

The drag and lift forces acting on the collection device supported using a bar were measured by a three-component strain gauge force balance (NISSHO-ELECTRIC-WORKS, LMC-3501-5), as shown in Fig. 4. The capacity of this sensor is 5 N, 5 N, and 5 N m for the drag, lift, and pitching moment, respectively, with an accuracy of 0.03%–0.05% of capacity. The signal was sampled at 1,000 Hz for 1 min and fed into the processing system via a signal conditioner (KYOWA, MCF-8A) and A/D converter (GRAPHTEC, GL7000-UM-802). The resolution of this system is 2.2×10^{-6} N for drag and lift, and 1.2×10^{-7} N m for the pitching moment. The wind speed was set to 3 and 5 m/s ($Re = 3.0 \times 10^4$ and 5.0×10^4). The maximum blockage ratio was 1.25% when the collection device and the approaching wind were orthogonal to each other. Because the aerodynamic forces acting on the support bar cannot be ignored, those acting on the support bar were separately measured by installing only the support bar in the force balance and subtracted from those acting on the whole system. The aerodynamic force coefficients were calculated using the following equations:

$$C_d = \frac{D_f}{0.5\rho U^2 A}, \quad C_l = \frac{L_f}{0.5\rho U^2 A} \quad (2)$$

where D_f is the drag force (N), L_f is the lift force (N), ρ is the air density (kg/m^3), U is the approaching wind speed (m/s), and A is the combined area of the gauze and wooden frame ($(0.15 \text{ m})^2 = 0.0225 \text{ m}^2$). The main flow direction component of the aerodynamic force is defined as the drag and the vertical direction component as the lift.

2.1.4 Measurement of pressure loss coefficients of gauze

The pressure loss that occurs when the airflow passes through a porous media can be calculated as the sum of viscous resistance and inertial resistance, as follows [28, 29]:

$$\Delta p / \Delta x = -(\mu D_n U + 0.5 \rho F_n U^2) \quad (3)$$

where Δp is the pressure loss (Pa), Δx is the length of the porous media (= gauze thickness) (m), U is the approaching wind speed (m/s), μ is the air viscosity coefficient (Pa·s), ρ is the air density (kg/m^3), D_n is the normal viscous resistance coefficient ($1/\text{m}^2$), and F_n is the normal inertial resistance coefficient ($1/\text{m}$). In this study, the flow field around the collection device was first calculated using the porous media model without considering the resistance in the tangential direction of the gauze based on Eq. (3). As D_n and F_n of Eq. (3) depend on the target material, we evaluated these coefficients of the gauze through wind tunnel tests.

The pressure loss of the gauze was measured with another Eiffel-type wind tunnel (test section of 200 mm in height, 200 mm in width, and 2,100 mm in total length), as shown in Fig. 5. This wind tunnel had a uniform wind speed distribution at the installation position of the gauze, and the turbulence intensity in the mainstream direction was 0.5% at a wind speed of 3 m/s. Two sheets of

gauze were installed in the wind tunnel, and the amount of pressure loss was measured because the gauze method uses two sheets of gauze, as described in the introduction. By connecting a tube to the pressure hole prepared in the wind tunnel wall, 30 mm away from the gauze, the pressure difference between the front and behind the gauze was measured with a differential pressure gauge (Okano Seisakusho, DMP 302N12). This differential pressure gauge has a maximum measurement range of 2 kPa, a resolution of 0.1 Pa, and an accuracy of $\pm 4.1\text{--}5.1$ Pa. The pressure loss was measured twice for 1 min at each approaching wind speed, that is, 1, 2, 3, 4, 5, and 6 m/s.

2.2 Flow field analysis method

This section describes the method of flow field analysis around a collection device using CFD. In this study, we calculated the unsteady flow field around the collection device using a large eddy simulation (LES) using OpenFOAM [30]. LES was adopted because the fine-scale eddies were expected to affect the behavior of particles near the collection device. The governing equations used were the filtered incompressible Navier–Stokes equations and the equation of continuity as follows:

$$\frac{\partial \bar{u}_i}{\partial x_i} = 0 \quad (4)$$

$$\frac{\partial \bar{u}_i}{\partial t} + \bar{u}_j \frac{\partial \bar{u}_i}{\partial x_j} = -\frac{1}{\rho} \frac{\partial \bar{p}}{\partial x_i} + \frac{\partial}{\partial x_j} \left\{ (\nu + \nu_{SGS}) \left(\frac{\partial \bar{u}_i}{\partial x_j} + \frac{\partial \bar{u}_j}{\partial x_i} \right) \right\} \quad (5)$$

where \bar{u}_i is the filtered velocity, \bar{p} is the filtered pressure, ν is the viscosity, ρ is the density, and ν_{SGS} is the subgrid eddy viscosity coefficient, which was modeled in this study by the Smagorinsky model [31] as follows:

$$\nu_{SGS} = (C_s f_s \Delta)^2 |\bar{D}| \quad (6)$$

where \bar{D} is the strain rate tensor, Δ is the filter width, f_s is the damping function that corrects the value of v_{SGS} near the wall, and C_s is the Smagorinsky constant, which was set to 0.12. Discretization was performed by the finite-volume method using collocated coordinates. The spatial difference was the second-order central difference, and the first-order implicit Euler method was used for the time advancement. All the simulations were conducted under smooth flow conditions, similar to the wind tunnel tests.

Fig. 6 shows the calculation domain. The thickness of the wooden frame was $0.12D$ ($= 18$ mm), where D is the outer size of the collection device ($= 150$ mm). The calculation area was $10D$ upstream, $20D$ downstream, and $10D$ vertically and horizontally from the collection device. This domain size was determined in accordance with Architectural Institute of Japan (AIJ) guidelines [32]. The boundary conditions are specified as follows: A smooth inflow was employed at the inlet as a boundary condition. On the outlet boundary, the gradient of the velocity in the streamwise direction and the pressure were zero. On the surrounding boundaries (except for the inlet, outlet, and collection device), slip-wall conditions were applied. On the wooden frame surfaces, a no-slip boundary condition was applied. The boundary condition for the gauze part is given by Eq. (3). The vertical size of the wall-adjacent grids was $D/400$ so that some grids should be located in the viscous sub-layer, and the total number of grids was approximately 10 million. The smooth inflows of 0.5, 1, 3, and 5 m/s were employed ($Re = 0.5 \times 10^4$, 1.0×10^4 , 3.0×10^4 , and 5.0×10^4). The approaching wind angle was set to 0° , 22.5° , 45° , and 67.5° . The wind direction was controlled through the angle of the collection device, as shown in Fig. 7. The dimensionless time increment ($U\Delta t/D$) of the

analysis was set between 3.3×10^{-4} and 1.0×10^{-3} depending on the analysis case, and the calculation was conducted for the dimensionless time $(Ut/D) = 400$ for all cases.

As a computational validation, this analysis domain and grid size were applied to the flow field analysis around a $150 \text{ mm} \times 150 \text{ mm}$ square plate with a depth of 7.5 mm ($\text{Re} = 5.0 \times 10^4$). The aerodynamic force coefficients could be obtained with a relative error of less than 1% compared to the previous experimental results by Tachikawa and Fukuyama [22]. Thus, the area and grid size were determined to be reasonable, and they were adopted for the flow field analyses around the collection device.

3 Experimental and numerical results

This section first describes the results of the PIV analysis around the collection device. Next, we show the experimental results of the pressure loss coefficient measurement of the gauze. Further, we present the results of the flow field analysis using CFD around the collection device and also incorporate the pressure loss coefficients. Finally, the wind speed near the device and aerodynamic force coefficients were validated by the corresponding wind tunnel tests.

3.1 Flow visualization through PIV analysis

Fig. 8 shows the time-averaged streamlines for 0° and 45° obtained by PIV. The streamlines were drawn based on the fourth-order Runge–Kutta method in a two-dimensional section. First, in

the case of 0° , a symmetrical recirculation region was formed behind the collection device, and this symmetrical recirculation region disappeared when the collection device and the approaching wind were not orthogonal. These phenomena correspond to those in a previous study of three-dimensional plates [33]. Additionally, airflows are perpendicular to the gauze at the backside, regardless of the approaching wind direction. This is because the airflow is rectified in the orthogonal axial direction of the gauze when the airflow passes through the gauze part. Valizadeh et al. [34] reported that as the porosity of the net structure decreases, the outflow direction from the net becomes perpendicular to the net surface. Because the gauze used in this study has a small porosity, it is presumed that the flow is completely rectified in the direction perpendicular to the gauze. Moreover, when the collection device has an angle of attack against the approaching wind, the airflows move along the front surface of the device. This is because the apparent density of the gauze increases and behaves as a wall with an increase in the approaching angle.

3.2 Measurement of pressure loss coefficients of the gauze

Fig. 9 shows the average and variations of the pressure loss measurements, together with an approximate curve determined by the least-squares method [35]. The figure also plots the amount of pressure loss estimated using a wire gauze in a previous study. Utsumi et al. [36] empirically derived an equation expressing the relationship between the approaching wind speed and pressure loss that can be applied to any wire gauze. The pressure loss values of this experiment and those of Utsumi et al. [36] were in good agreement, and the relative error was 7% at a wind speed of 6 m/s, confirming the validity of this experiment. From this approximate function, the pressure loss

coefficient in Eq. (3) was determined to be $D_n = 4.65 \times 10^5$ and $F_n = 5.62$. In the subsequent flow field analysis around the collection device using CFD, these pressure loss coefficients were incorporated as the boundary condition at the gauze.

3.3 Flow field around the collection device obtained using CFD without considering the tangential resistance of the gauze

Fig. 10 shows the time-averaged wind speed for 0° and 45° during the dimensionless time $Ut/D = 200\text{--}400$ with an approaching wind speed of 1 m/s. In particular, Figs. 10(a) and (b) show the flow field in the case where the tangential resistance of the gauze was not considered. These figures show that the wind speed gradually decreased near the collection device as a result of the resistance of the gauze modeled by the porous media model, and then the flow passed through the gauze part. Moreover, in the instance where the collection device has an angle of attack against the approaching flow, the approaching air flowed down along the front surface of the device. These results are qualitatively consistent with the results obtained by PIV analysis. However, the flow behind the gauze was not rectified to the normal direction of the gauze, unlike the PIV analysis results.

Fig. 11 compares the experimental and numerical results of wind speed in the vicinity of the collection device. First, the measured wind speed tends to increase at the windward side of the gauze and decreases at the leeward side as the wind angle becomes large. As observed from the visualization tests, this occurs because the approaching air flowed down along the front surface of the device when the device has an angle of attack against the approaching wind, thereby reducing the flows that travel through the gauze to reach the leeward side. Additionally, regardless of wind

direction, the approaching wind speed and the wind speed near the gauze have a non-linear relationship, which is likely to influence the collection efficiency of the gauze method. However, there are discrepancies between the numerical and experimental values, especially for the 45° and 67.5° cases on the leeward side. This is also probably because the airflow was not rectified at the gauze.

Fig. 12 compares the experimental and numerical results of the aerodynamic force coefficients. The dependence of the aerodynamic force coefficients on the Reynolds number (Re) was small for both the experimental and numerical results, similar to previous studies of three-dimensional plates [22]. In the case of 0° , where the approaching wind is orthogonal to the device, the numerical and measured values of the drag force coefficient were almost the same and the relative error was 0.2% at $Re=50,000$. However, in the case of 22.5° and 45° , which has an angle of attack to the approaching wind, the numerical values of the drag and lift force coefficients were smaller than the measured values. On the other hand, in the case of 67.5° , the numerical and measured values of the drag and lift force coefficients were almost the same and the relative error was less than 7% at $Re=50,000$. In this case, the aerodynamic force acting on the collection device is likely identical to the aerodynamic force acting only on the wooden frame of the device. That is, when the wind direction has an angle of 67.5° , the aerodynamic force acting on the gauze is very small, compared to the aerodynamic force acting on the entire collection device. These results suggest that the aerodynamic forces acting on the gauze have not been properly evaluated when the approaching wind is not orthogonal to the device.

In the above analysis, only the pressure loss in the direction perpendicular to the gauze plane was measured, and the resistance in the tangential direction of the gauze was not considered. However, it was not possible to reproduce the experimental values accurately, especially in the case where the collection device and the approaching wind were not orthogonal.

In the next section, an analysis considering the tangential and normal resistances of the gauze is conducted and compared with the results of the wind tunnel tests.

3.4 Flow field around the collection device obtained using CFD with the tangential resistance of the gauze

To consider the tangential resistance of the gauze, the relation between the wind speed and the pressure loss caused by the porous media is expanded in three dimensions as follows [21, 37]:

$$\partial p / \partial x_i = -(\mu D_{ij} + 1/2 \rho |u| F_{ij}) u_j \quad (7)$$

$$D_{ij} = \begin{pmatrix} D_n & 0 & 0 \\ 0 & D_t & 0 \\ 0 & 0 & D_t \end{pmatrix} \quad (8)$$

$$F_{ij} = \begin{pmatrix} F_n & 0 & 0 \\ 0 & F_t & 0 \\ 0 & 0 & F_t \end{pmatrix} \quad (9)$$

Here, D_n is the normal viscous resistance coefficient, D_t is the tangential viscous resistance coefficient, F_n is the normal inertial resistance coefficient, and F_t is the tangential inertial resistance coefficient. To represent the tangential resistance of the gauze, D_t and F_t must be set appropriately. However, because of the thin structure, measuring D_t and F_t by wind tunnel tests is difficult. Maruyama [37] performed a flow field analysis around a windbreak under the assumption that the

tangential resistance coefficients of a windbreak were the same as the normal resistance coefficients and obtained reasonable results compared to the experimental ones. Therefore, based on this result, the tangential resistance coefficients D_t and F_t of the gauze were set to $D_t = D_n = 4.65 \times 10^5$ and $F_t = F_n = 5.62$. The validity of this assumption is discussed below.

Figs. 10(c) and (d) show the time-averaged flow fields with an approaching wind speed of 1 m/s when the tangential resistance of the gauze was considered. In all wind directions, the airflow was rectified in the orthogonal direction at the leeward side. These results are qualitatively consistent with those obtained by PIV analysis. Additionally, even if the tangential resistance coefficients of the gauze were set to 10 times larger than the normal resistance coefficients ($D_t = 4.65 \times 10^6$, $F_t = 56.2$), the flow fields were qualitatively consistent with the PIV analysis results. On the other hand, if the tangential resistance coefficients were set to 10 times smaller than the normal resistance coefficients ($D_t = 4.65 \times 10^4$, $F_t = 0.562$), the airflow was not rectified in the orthogonal direction of the gauze, similar to the analysis without considering the tangential resistance. Therefore, although the minimum threshold value of the tangential resistance coefficients of the gauze that can reproduce the PIV results should be investigated in the future, sufficiently large tangential resistance coefficients can express the effect of rectifying the airflow by the gauze. As a conclusion, the porous media model can be applied to the gauze, which is a very thin structure with a small porosity, by considering the tangential resistance appropriately.

Next, to evaluate the validity of the flow fields quantitatively, the analyzed values of wind speed near the device and aerodynamic force coefficients were compared with the measurement results.

Fig. 13 shows the numerical results of the 9-point averaged wind speed in the vicinity of the

collection device. The numerical and measured values of wind speed in the vicinity of the device were almost the same in all wind directions on both the front and backside of the gauze. On the windward side of the gauze, the relative error was 7.0% at 0° , 2.5% at 22.5° , 5.1% at 45° , and 6.6% at 67.5° for the approaching wind speed of 5 m/s. On the leeward side, the relative error was 5.6% at 0° , 5.1% at 22.5° , 6.8% at 45° , and 9.6% at 67.5° . Thus, the wind conditions around the collection device could be accurately reproduced by considering the tangential resistance of the gauze.

Fig. 14 shows the numerical results of the aerodynamic force coefficients of the device when considering the tangential resistance of the gauze. The numerical and measured aerodynamic force coefficients were almost the same for all angles of attack. The maximum relative error was 7.7% for the drag force coefficient and 8.9% for the lift force coefficient at $Re=50,000$. That is, the force acting on the gauze can be evaluated appropriately by setting the tangential resistance coefficients of the gauze.

Fig. 15 shows a comparison of the time-averaged wind speeds in the mainstream direction at the center height of the collection device for 0° and 45° obtained through PIV and CFD. The sampling frequency of the wind speed data for both CFD and PIV was set to 300 Hz. First, in the case of 0° , the wind speed distribution was symmetrical to a vertical plane of $y/D = 0$, which was a reasonable result. For both PIV and CFD, a negative wind speed was observed for $x/D \geq 0.4$ at 0° and $x'/D \geq 0.2$ at 45° , suggesting that CFD has a reasonable flow field from the viewpoint of the generation of a wake. Fig. 16 shows a comparison of the Reynolds stress ($-\overline{u'v'}/U^2$) at the center height of the collection device. Large turbulent stresses occurred in the region of separation flows from the wooden frame for both 0° and 45° . This corresponds to the phenomenon that the turbulence

intensity is greatest around the edge in the net structure [23]. Additionally, in the case of 45°, extremely large turbulent stresses occurred in the recirculation region behind the wooden frame, and CFD accurately captured this phenomenon. Thus, the validity of the CFD results was confirmed in terms of both the time-averaged and the variable components.

As mentioned above, it was clarified that the flow field around the collection device can be calculated quantitatively by considering the tangential and normal resistances of the gauze. This result suggests that the tangential resistance must be considered in the porous media model when the porosity of the objects is small, even if the thickness is small, such as gauze. Subsequently, the particle scattering analysis was performed using the calculated flow fields to evaluate the particle behavior in the vicinity of the collection device and to calculate the arrival rate of particles at the gauze.

4 Particle scattering analysis of the collection device

Using the flow field obtained by CFD, the arrival rate (α) of particles to the gauze part was calculated. This section first provides an overview of the particle scattering analysis. Then, we show the results of the analysis and discuss the effects of the wind speed, wind direction, and particle size on the arrival rate (α).

4.1 Particle scattering analysis

Particles in a fluid move because of fluid resistance, gravity, buoyancy, and added mass force [38]. In general, the forces acting on particles except for drag and gravity can be ignored in the case of $\rho_p/\rho_f > 10^3$, where ρ_p is the particle density and ρ_f is the fluid density [39, 40]. The typical sea-salt-particle density value of $\rho_p = 1.11 \times 10^3 \text{ kg/m}^3$ [41] satisfies the criteria above. Furthermore, to discuss the effect of the fluid on the movement of particles around the device, we also neglected gravity to consider only the effects of the drag. Hence, the equation of motion of a particle is expressed by Eq. (10) [42]:

$$m_p \frac{d\mathbf{u}_p}{dt} = 1/8 C_{dp} \pi d_p^2 \rho_f (\mathbf{u}_f - \mathbf{u}_p) |\mathbf{u}_f - \mathbf{u}_p| \quad (10)$$

where m_p is the particle mass (kg), \mathbf{u}_p is the particle velocity vector (m/s), \mathbf{u}_f is the fluid velocity vector (m/s), C_{dp} is the drag coefficient of a spherical particle, d_p is the particle diameter (m), and ρ_f is the air density (kg/m^3). The drag coefficient of a spherical particle C_{dp} is expressed by the following equation based on a previous study [43]:

$$C_{dp} = \begin{cases} \frac{24}{\text{Re}_p} \left(1 + \frac{1}{6} \text{Re}_p^{\frac{2}{3}} \right) & \text{Re}_p \leq 1000 \\ 0.424 & \text{Re}_p > 1000 \end{cases} \quad (11)$$

where Re_p is the particle Reynolds number, defined by the diameter of a particle.

To solve the equation of motion for particles given by Eq. (10), the fluid velocity \mathbf{u}_f at the particle position is necessary. In this analysis, the fluid velocity \mathbf{u}_f at a particle position was interpolated from the fluid velocity at the cell center obtained in the flow field calculation. Herein, the behavior of a particle in the vicinity of the collection device was analyzed by scattering particles in the same calculation domain of the flow field analysis. The initial position of the particles was $3D$ (D : outer

size of the collection device) upstream from the gauze surface. In advance, we investigated the relationship between the initial position of the particles and the arrival rate by varying their initial positions and found that there was no difference in the arrival rate for all angles of attack if the initial position of the particles was more than $3D$ upstream of the collection device. We set the particle density to $1.11 \times 10^3 \text{ kg/m}^3$ and particle diameters of 2, 20, and 200 μm , referring to a previous study [41]. Additionally, to investigate the effect of gravity acting on particles, some preliminary calculations of particle scattering were conducted under the condition of a particle size of 200 μm and an approaching wind speed of 0.5 m/s, where the effect of gravity was relatively larger than that in other cases. This clarified that the difference in the arrival rate (α) between cases with and without gravity was only 3%. In addition, when considering gravity, a greater number of particles must be placed in the vertical direction to evaluate the vertical movements of particles because of gravity, resulting in a high computational cost. Thus, gravity was also neglected to reduce the computational cost and to study the fundamental effects of the flow field on the behavior of particles near the collection device. As mentioned in the introduction, the capture rate was set to $\beta = 1$, indicating that all particles arriving at the gauze surface should be captured by the strings of the gauze, thereby preventing any particles from passing through the gauze. Moreover, a particle arriving at the surface of the device is supposed not to bounce and fall down.

4.2 Results and discussion of particle scattering analysis

Fig. 17 shows the calculation results of the percentage of particles reaching the gauze. The ratio of 1 indicates that all particles coming from upstream reached the gauze part. By observing the

relationship between the arrival ratio and the approaching wind speed or the arrival rate and the particle size in all wind directions, the arrival ratio becomes larger with an increase in the approaching wind speed or particle size. This is because a greater wind speed and larger particle size result in a larger inertial force. Thus, a greater number of particles reach the gauze. Additionally, for example, in the case of the wind direction of 0° , the arrival rate at the approaching wind speed of 5 m/s was approximately 5.7 times larger than that of 0.5 m/s for $2\ \mu\text{m}$, approximately 5.6 times larger for $20\ \mu\text{m}$, and approximately 2 times larger for $200\ \mu\text{m}$. Therefore, the amount of salt obtained by the gauze method must be carefully interpreted considering the large difference in the arrival rate against the wind speed. Furthermore, comparing the arrival rates of the different particle sizes, the arrival rates of $2\ \mu\text{m}$ and $20\ \mu\text{m}$ were approximately the same at all wind speeds and directions, while that of $200\ \mu\text{m}$ was approximately 1.2 to 6.2 times larger than for $2\ \mu\text{m}$ and $20\ \mu\text{m}$, depending on the wind speed and direction. Although the distribution of airborne salt particle size has a peak around $1\text{--}10\ \mu\text{m}$ [44], larger particles can be observed near the coastal line. Thus, considerable attention should be paid to appropriately considering the arrival rate, especially in coastal areas.

The arrival ratio of particles also increases with an increase in the wind angle. This corresponds to the fact that the wind speeds in the main flow direction near the gauze becomes large as the wind direction increases, which was clarified by the wind speed measurement test. Additionally, the arrival ratio of particles at the gauze exhibited an asymptotic trend against the wind speed. This occurred because the particles flying far away from the center of the gauze, that is, close to the wooden frame, tend to avoid the collection device even if the wind speed becomes large. They also tend to be transported by the airflow that flows down without reaching the gauze part. Furthermore,

the arrival rate is most sensitive to changes in wind speed when the collection device is orthogonal to the approaching wind and becomes insensitive as the angle of attack increases. The difference in arrival rate between the wind directions was especially prominent at lower wind speeds. For example, the arrival rate of 2 μm for the approaching wind speed of 0.5 m/s at 67.5° was approximately eight times greater than that at 0°, while that for 5 m/s was two times greater. Therefore, when the gauze method is used in places where wind speed is expected to be low, such as inside a bridge girder, special attention should be paid to the effect of wind direction.

Additionally, it was expected that the wind speed near the collection device was significantly related to the arrival rate of particles; therefore, we investigated the relationship between the arrival rate and the wind speed ratio, which was defined as the ratio between the approaching wind speed and gauze-surface wind speed. The gauze-surface wind speed in this study was defined as the wind speed averaged over a gauze surface of 100 mm \times 100 mm in the windward side. Fig. 17 also shows the wind speed ratio as a dotted line for each angle of attack, together with the arrival rate. The arrival rate of particles and the wind speed ratio were in good agreement when the particle sizes were 2 μm and 20 μm . This is because the inertial force acting on the particles is sufficiently small to have a great ability to follow the fluid. However, in the case of 200 μm , the arrival rate was higher than the wind speed ratio. This is because the large inertial force acting on the particles does not follow the fluid motion.

From these results, when large particles are not transported as in inland areas, the arrival rate of the particles can be estimated by evaluating the gauze-surface wind speed without conducting particle scattering analysis. On the other hand, if the gauze method is used near the coastline, where

large particles are expected to be observed, particle scattering analysis must be conducted to evaluate the arrival rate.

As clarified above, the percentage of particles arriving at the gauze part changes depending on the wind speed, wind direction, and salt particle size. That is, not only the approaching wind speed but also the wind direction must be considered when evaluating the amount of airborne salt particles using the gauze method. As mentioned in Section 1, Obata and Murakami reported that collection efficiency varies depending on the observation period by outdoor observations [12]. They also reported that the collection efficiency differs greatly depending on the observation period, even when the period-averaged wind speed in the direction perpendicular to the device was at the same level. This result probably comes from the fact that the collection efficiency depends not only on the wind speed but also on the wind direction, as clarified in the present study. Additionally, the collection efficiency based on the wind speed and direction changes with time, which affects the period-averaged collection efficiency. In the future, it would be interesting to calculate the collection efficiency based on the time series wind speed and direction data and compare it with the observation results.

Additionally, a criterion for using weathering steel without coating is regulated based on the amount of airborne salt in the atmosphere, which is evaluated by devices such as the gauze method, as mentioned in Section 1. In other words, the amount of airborne salt obtained by the gauze method has been related to the amount of corrosion of steel by previous on-site observations [2]; thus, the gauze method is used as an index for the maintenance of structures. However, the gauze method does not represent the true salinity environment of the installation site because the arrival rate of

particles is not 100% ($\alpha = 1$), as revealed in this study. In the future, by clarifying the capture rate by gauze fibers (β), it will be possible to calculate the true airborne salt content by observing the wind conditions at the location where the gauze method is installed. The amount of salt adhering to any point of a structure such as a bridge can then be quantitatively evaluated by conducting a particle scattering analysis based on the flow fields around the structure using the calculated salt concentration from the gauze method as an input value. The quantitative prediction of the amount of salt adhering to the surface of a structure will contribute to effective maintenance and management of structures.

5 Concluding remarks

In this study, as a first step to clarify the collection efficiency of the dry gauze method, we simulated the flow field around the collection device using CFD with the porous media model. Then, particle tracking was performed in the calculated flow field, and the collection efficiency was evaluated under the condition of a filtration efficiency of 100%. The conclusions are as follows:

- Instead of accurately reproducing the gauze structure in CFD, we adopted the porous media model for the gauze. The flow fields were reproduced well in all the wind directions investigated in this study using the porous media model, which considered both the tangential and normal resistances of the gauze. This result suggests that the tangential resistance must be considered in

the porous media model when the porosity of an object is small, even if the thickness is small, such as with gauze.

- The approaching wind speed and the wind speed near the gauze have a non-linear relationship. Therefore, the collection efficiency of the gauze method needs to be investigated for each wind speed. Wind direction is also important because if the device has an angle of attack against the approaching wind, the apparent density of the gauze increases, and the gauze behaves as if it is a wall.
- The arrival rate of the particles was quantitatively evaluated considering wind speed, wind direction, and salt particle size. In the case of small particles of 2 μm and 20 μm , the arrival rates were similar, but the arrival rate of large 200 μm particles was dramatically larger than that of small particles. Thus, considerable attention should be paid, especially in coastal areas, where large particles are expected to be observed, to appropriately consider the arrival rate. Furthermore, the difference in the arrival rate between the wind directions was especially prominent at lower wind speeds. Therefore, when the gauze method is used in places where wind speed is expected to be low, including inside a bridge girder, special attention should be paid to the effect of the wind direction. Additionally, because the arrival rate varies significantly depending on wind conditions, we should interpret the amount of airborne salt obtained by the gauze method while considering the wind conditions, which has not been considered in previous studies.
- When large particles are not supposed to be transported such as at an inland area, the arrival rate of the particles can be estimated by evaluating the gauze-surface wind speed without conducting

the particle scattering analysis. This is because the inertial force acting on the particles is sufficiently small to have a great followability in the fluid. On the other hand, if the gauze method is used near the coastline, where large particles are expected to be observed, particle scattering analysis needs to be conducted to evaluate the arrival rate.

Herein, we analyzed the behavior of particles around the collection device and ascertained the relationship between the wind conditions and the proportion of particles reaching the gauze part. In future work, to realize an accurate evaluation of airborne salt content by gauze method, the amount of salt particles collected by each fiber of the gauze should be discussed in detail by calculating the movement of a particle around the gauze fiber using CFD.

ACKNOWLEDGMENTS

This work was partially supported by JSPS KAKENHI Grant Number 15H02261 and 18K13820. The supercomputer of ACCMS, Kyoto University, was used for the flow simulation.

REFERENCES

- [1] Ministry of Land, Infrastructure, Transport, and Tourism (MLITT), 2008, “Survey on the Replacement of Bridges IV,” Accessed January 15, 2021. [In Japanese]
<http://www.nilim.go.jp/lab/bcg/siryou/tnn/tnn0444pdf/ks0444.pdf>
- [2] Japan Road Association (JRA), 2012, “Specification for Highway Bridges, II (Steel bridge),” Tokyo.
- [3] Manders, A. M. M., Schaap, M., Querol, X., Albert, M. F. M. A., Vercauteren, J., Kuhlbusch, T. A. J., and Hoogerbrugge, R., 2010, “Sea Salt Concentrations Across the European Continent,” *Atmos. Environ.* **44**(20), pp. 2434–2442. DOI: 10.1016/j.atmosenv.2010.03.028.
- [4] Noguchi, K., Shirato, H., and Yagi, T., 2017, “Numerical Evaluation of Sea Salt Amounts Deposited on Bridge Girders,” *J. Bridge Eng.* **22**(7): 04017021.
DOI: 10.1061/(ASCE)BE.1943-5592.0001061.
- [5] Cooperative Research Centre for Construction Innovation (CRCCI), 2005, “Case-Based Reasoning in Construction and Infrastructure Projects - Final Report,” Rep. No. 2002-059-B No. 16, Brisbane, Australia.
- [6] Zhou, M., Liao, J., and An, L., 2020, “Effect of Multiple Environmental Factors on the Adhesion and Diffusion Behaviors of Chlorides in a Bridge with Coastal Exposure: Long-Term Experimental Study,” *J. Bridge Eng.* **25**(10): 04020081. DOI: 10.1061/(ASCE)BE.1943-5592.0001614.
- [7] Tørseth, K., Hanssen, J.E., and Semb, A., 1999, “Temporal and Spatial Variations of Airborne Mg, Cl, Na, Ca and K in Rural Areas of Norway,” *Sci. Total Environ.* **234**, pp. 75–85.
DOI: 10.1016/S0048-9697(99)00261-2.
- [8] ISO 9225, 2012, “Corrosion of Metals and Alloy-Corrosivity of Atmospheres-Measurement of Pollution.” International Organization for Standardization.
- [9] Public Works Research Institute (PWRI), 1993, “Nation-Wide Investigation on Air-borne Chloride (4) Relationship Between Geographical Distribution of Air-borne Chloride and Wind,” [In Japanese] Technical Memoranda of PWRI 3175, Tsukuba, Japan.
- [10] Japanese Industrial Standards (JIS), 1998, “Determination of Pollution for Evaluation of Corrosivity of Atmospheres,” Japanese Industrial Standards Committee, Tokyo.
- [11] Takebe, M., Ohya, M., Hirose, N., Adachi, R., Ago, Y., Doi, K., Iwatani, Y., Kitagawa, N., Kimura, Y., Ochibe, K., and Ota, J., 2010, “Difference in Precipitation Rates of Air-borne Salts Collected by the Dry Gauze Method and the Doken Tank Method,” *Corros. Sci.* **52**, pp. 2928–2935.

DOI: 10.1016/j.corsci.2010.05.004.

[12] Obata, M., and Murakami, T., 2014, “Observation of Suspended Sea Salt Particles and Its Numerical Simulation as Estimation of Corrosive Environment,” *J. Struct. Eng.* **60A**, pp. 596–604. [In Japanese] DOI: 10.11532/structcivil.60A.596.

[13] Basnet, K., Constantinescu, G., Muste, M., and Ho, H., 2015, “Method to Assess Efficiency and Improve Design of Snow Fences,” *J. Eng. Mech.* **141**(3):04014136. DOI: 10.1061/(ASCE)EM.1943-7889.0000871.

[14] Baniamerian, Z., and Mehdipour, R., 2017, “Studying Effects of Fence and Sheltering on the Aerodynamic Forces Experienced by Parabolic Trough Solar Collectors,” *ASME. J. Fluids Eng.* **139**(3): 031103. DOI: 10.1115/1.4034951

[15] Kizilaslan, M. A., Nasyrlayev, N., Kurumus, A. T., Savas, H., Demirel, E., and Aral, M. M., 2020, “Experimental and Numerical Evaluation of a Porous Baffle Design for Contact Tanks,” *J. Environ. Eng.*, **146**(7): 04020063. DOI: 10.1061/(ASCE)EE.1943-7870.0001747.

[16] Andrzej, K., and Joanna, Ł., 2009, “Experimental and Modelling Study on Flow Resistance of Wire Gauzes,” *Chem. Eng. Process.-Process Intensif.* **48**, pp. 816–822. DOI: 10.1016/j.cep.2008.10.009.

[17] Giannoulis, A., Mistriotis, A., and Briassoulis, D., 2010, “Experimental and Numerical Investigation of the Airflow Around a Raised Permeable Panel,” *J. Wind Eng. Ind. Aerodyn.* **98**, pp. 808–817. DOI: 10.1016/j.jweia.2010.07.005.

[18] Fan, J., Lominé, F., and Hellou, M. 2020, “Numerical Investigation of the Influence of Fiber Geometry on Filtration Performance With a Coupled Lattice Boltzmann–Discrete Element Method,” *ASME. J. Appl. Mech.* **87**(1): 011005. DOI: 10.1115/1.4044928.

[19] Kuroyanagi, T., 2017, “Investigating Air Leakage and Wind Pressure Coefficients of Single-Span Plastic Greenhouses Using Computational Fluid Dynamics,” *Biosyst Eng.* **163**, pp. 15–27. DOI: 10.1016/j.biosystemseng.2017.08.004.

[20] Noda, M., Teramoto, S., Akagi, K., and Nagao F., 2014, “Decision Method of Pressure Loss Coefficient of Windbreak Nets for CFD,” *Proc., 23rd National Symp. on Wind Engineering*, pp. 445–450. [In Japanese] DOI: 10.14887/kazekosymp.23.0_445.

[21] Mahgoub, A. O., and Ghani, S., 2021, “Numerical and Experimental Investigation of Utilizing the Porous Media Model for Windbreaks CFD Simulation,” *Sustain. Cities Soc.* **65**. DOI: 10.1016/j.scs.2020.102648.

- [22] Tachikawa, M., and Fukuyama, M., 1981, “Trajectories and Velocities of Typhoon-Generated Missiles, Part 1: Aerodynamic Characteristics of Flat Plates and Equations of Motion,” *Trans. AIJ* **302**, pp. 1–11. [In Japanese] DOI: 10.3130/aajsaxx.302.0_1.
- [23] Tomisaka, K., and Maruyama, T., 2007, “Measurement of the Aerodynamic Characteristics of a Net,” *J. Wind Eng.* **32**, pp. 103–112. [In Japanese] DOI: 10.5359/jwe.32.103
- [24] Løland, G., 1993, “Current Forces on, and Water Flow Through and Around, Floating Fish Farms,” *Aquacult. Int.* **1**, pp. 72–89. DOI: 10.1007/BF00692665.
- [25] Honshu-Shikoku Bridge Authority, 2001, “Wind Resistant Design Standard for Honshu–Shikoku Bridges,” Honshu–Shikoku Bridge Authority, Japan.
- [26] Giovannetti, L. M., Banks, J., Turnock, S. R., and Boyd, S. W., 2017, “Uncertainty Assessment of Coupled Digital Image Correlation and Particle Image Velocimetry for Fluid-Structure Interaction Wind Tunnel Experiments,” *J. Fluids Struct.* **68**, pp. 125–140. DOI: 10.1016/j.jfluidstructs.2016.09.002.
- [27] The Visualization Society of Japan, 2002, *Handbook of particle image velocimetry*, Morikita, Tokyo.
- [28] Straatman, A. G., Gallego, N. C. Yu, Q., Thompson B. E., 2006, “Characterization of Porous Carbon Foam as a Material for Compact Recuperators,” *J. Eng. Gas Turbines Power* **129**(2), pp. 326–330. DOI: 10.1115/1.2436562.
- [29] Hong, S. W., Lee, I. B., and Seo, I. H., 2015, “Modelling and Predicting Wind Velocity Patterns for Windbreak Fence Design,” *J. Wind Eng. Ind. Aerodyn.* **142**, pp. 53–64. DOI: 10.1016/j.jweia.2015.03.007.
- [30] OpenFOAM, 2017, *The Open Source CFD Toolbox. User Guide Version 4.0*, the OpenFOAM Foundation, accessed April 2, 2021, <https://openfoam.org/version/4-0/>
- [31] Smagorinsky, J., 1963, “General Circulation Experiments with the Primitive Equations,” *Mon. Weather Rev.* **91**(3), pp. 99–164. DOI: 10.1175/1520-0493(1963)091<0099:GCEWTP>2.3.CO;2.
- [32] Tominaga, Y., Mochida, A., Yoshie, R., Kataoka, H., Nozu, T., Yoshikawa, M., and Shirasawa, T., 2008, “AIJ Guidelines for Practical Applications of CFD to Pedestrian Wind Environment Around Buildings,” *J. Wind Eng. Ind. Aerodyn.* **96**, pp. 1749–1761. DOI: 10.1016/j.jweia.2008.02.058.

- [33] Cadot, O., 2016, “Stochastic Fluid Structure Interaction of Three-Dimensional Plates Facing a Uniform Flow,” *J. Fluid Mech.* **794**, R1. DOI: 10.1017/jfm.2016.187.
- [34] Valizadeh, A., and Rudman, M., 2017, “A numerical approach for simulating flow through thin porous media,” *Eur. J. Mech. B Fluids* **65**, pp. 31–44.
DOI: 10.1016/j.euromechflu.2017.03.004.
- [35] Tsubokura, Y., Ishiwatari, J., Tokumasu, H., Shirato, H., Noguchi, K., and Yagi, T., 2018, “Evaluation of Salt Particle Behavior Around Device of Dry Gauze Method by CFD,” *Proc., 25th National Symp. on Wind Engineering*, pp. 157–162. [In Japanese]
DOI: 10.14887/kazekosymp.25.0_157.
- [36] Utsumi, R., Yamamoto, H., and Ichikawa, M., 1991, “Pressure drop of fluid flow through electroformed sieve,” *Kagaku Kougaku Ronbunshu* 17(2), pp. 341–346. [In Japanese]
DOI:10.1252/kakoronbunshu.17.341.
- [37] Maruyama, T., 2008, “Large Eddy Simulation of Turbulent Flow Around a Windbreak,” *J. Wind Eng. Ind. Aerodyn.* **96**, pp. 1998–2006. DOI: 10.1016/j.jweia.2008.02.062.
- [38] Greifzua, F., Kratzscha, C., Forgerb, T., Lindnera, F., and Schwarzea, R., 2016, “Assessment of Particle-Tracking Models for Dispersed Particle-Laden Flows Implemented in OpenFOAM and ANSYS FLUENT,” *Eng. Appl. Comput. Fluid Mech.* **10**(1), pp. 30–43.
DOI: 10.1080/19942060.2015.1104266.
- [39] Corrsin, S., and Lumley, J., 1956, “On the Equation of Motion for a Particle in Turbulent Fluid,” *Appl. Sci. Res.* **A6**, pp. 114–116.
- [40] Kurose, R., Makino, H., and Komori, S., 2002, “Fluid Forces on a Particle in Air Flows,” *J. Soc. powder Technol., Japan*, **39**, pp. 353–361. [In Japanese] DOI: 10.4164/sptj.39.353.
- [41] Kato, H., and Akai, Y., 2001, “A simple Model for Estimating the Amount of Wind-Driven Sea Salt Over Coastal Area,” *J. Agric. Meteorol.* **57**(2), pp. 79–92. [In Japanese]
DOI: 10.2480/agrmet.57.79.
- [42] Heinrich, M., and Schwarze, R., 2020, “3D-Coupling of Volume-of-Fluid and Lagrangian Particle Tracking for Spray Atomization Simulation in OpenFOAM,” *SoftwareX* **11**, 100483. DOI: 10.1016/j.softx.2020.100483.
- [43] Putnam A., 1961, “Integrable Form of Droplet Drag Coefficient,” *ARS J.* **31**(10), pp. 1467–1468.

[44] Athanasopoulou, E., Tombrou, M., Pandis, S. N., and Russell, A. G., 2008, “The role of sea-salt emissions and heterogeneous chemistry in the air quality of polluted coastal areas,” *Atmos. Chem. Phys.*, **8**, 5755–5769. DOI: 10.5194/acp-8-5755-2008, 2008.

Figure Captions List

- Fig. 1 Collection device of the gauze method: (a) schematic (unit: mm), (c) actual device, and (c) a device mounted under a bridge girder.
- Fig. 2 Setup of the PIV test: (a) installation condition of the collection device in the wind tunnel, (b) the wing-type smoke diffuser, and (c) camera position and irradiation direction of the laser.
- Fig. 3 Wind speed measurement near the collection device: (a) setup of measurement and (b) measurement points (the black circles show the measurement points of wind speed, unit: mm).
- Fig. 4 Setup of aerodynamic force coefficient measurements.
- Fig. 5 A schematic of wind tunnel used for measurement of pressure loss coefficients of gauze (unit: mm).
- Fig. 6 Calculation domain: (a) whole analysis area and (b) grids near the collection device.
- Fig. 7 Calculation grids for the flow field around the collection device with an angle of attack (angle of attack of 45°).
- Fig. 8 PIV analysis results of the time-averaged streamline at the center height around the collection device (the wind tunnel velocity is 1 m/s): (a) wind direction 0° , (b) 45° .
- Fig. 9 Comparison of pressure loss values obtained in this experiment with estimated values based on the study by Utsumi et al. [36].
- Fig. 10 Time-averaged flow fields at the center height around the collection device for 0° and 45° (wind velocity is 1 m/s): (a)(b) the wind speed by CFD without the

tangential resistance of gauze, (c)(d) the wind speed by CFD with the tangential resistance of gauze.

Fig. 11 Comparison of measured and analyzed values of 9-point averaged wind speeds near the gauze without considering the tangential resistance of the gauze: (a) front of the gauze and (b) back of the gauze. The error bars correspond to the standard deviation of the wind speed.

Fig. 12 Comparison of measured and analyzed aerodynamic force coefficients of the collection device without considering the tangential resistance of the gauze: (a) drag force coefficient and (b) lift force coefficient. The error bars correspond to the standard deviation of the aerodynamic force coefficients.

Fig. 13 Comparison of measured and analyzed values of 9-point averaged wind speeds near the gauze when considering the tangential resistance of the gauze: (a) front of the gauze and (b) back of the gauze. The error bars correspond to the standard deviation of the wind speed.

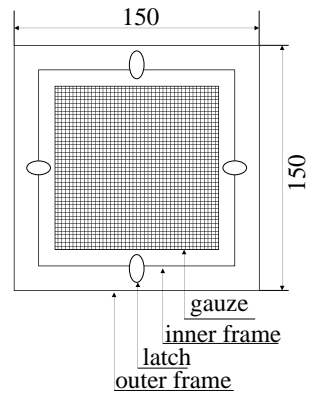
Fig. 14 Comparison of measured and analyzed aerodynamic force coefficients of the collection device when considering the tangential resistance of the gauze: (a) drag force coefficient and (b) lift force coefficient. The error bars correspond to the standard deviation of the aerodynamic force coefficients.

Fig. 15 Comparison of the time-averaged wind speed in the mainstream direction obtained by PIV and LES (approaching wind speed is 1 m/s): (a) Wind direction 0° and (b) 45° . Here, u is the streamwise wind speed, which is made dimensionless by the approaching wind speed U .

Fig. 16 Comparison of the Reynolds stress $(-\overline{u'v'})/U^2$ obtained by PIV and LES (approaching wind speed is 1 m/s): (a) Wind direction 0° and (b) 45° . Here, u'

is the fluctuating streamwise wind speed, and v' is the fluctuating transverse wind speed.

Fig. 17 Analysis results of the arrival rate of particles to the gauze part (α). Particle diameter: (a) 2 μm , (b) 20 μm , and (c) 200 μm . Here, the solid line represents the approximate curve of the arrival rate, and the dotted line represents the wind speed ratio between the approaching wind speed and gauze-surface wind speed.



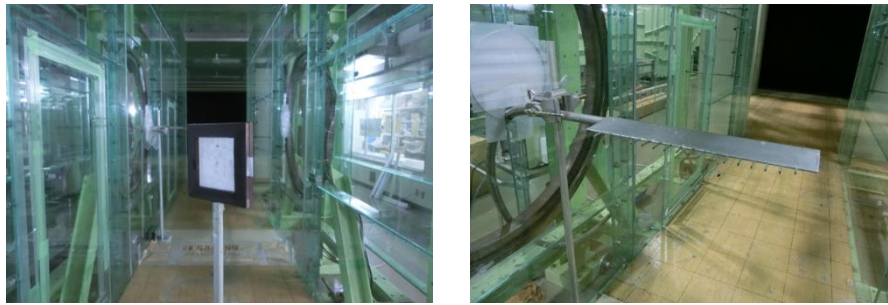
(a)

(b)



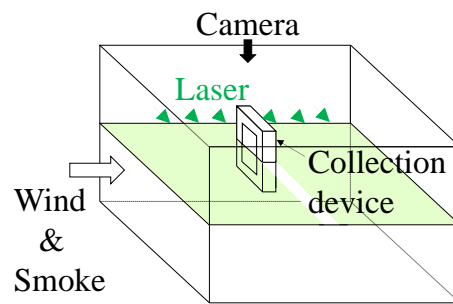
(c)

Fig. 1 Collection device of the gauze method: (a) schematic (unit: mm), (b) actual device, and (c) a device mounted under a bridge girder.



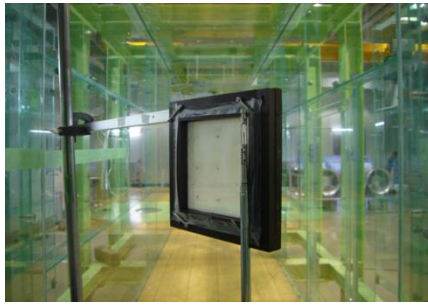
(a)

(b)

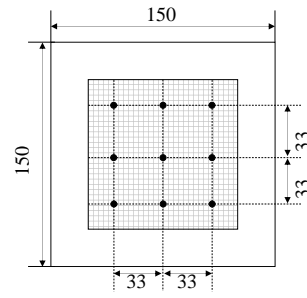


(c)

Fig. 2 Setup of the PIV test: (a) installation condition of the collection device in the wind tunnel, (b) the wing-type smoke diffuser, and (c) camera position and irradiation direction of the laser.



(a)



(b)

Fig. 3 Wind speed measurement near the collection device: (a) setup of measurement and (b) measurement points (the black circles show the measurement points of wind speed, unit: mm).



Fig. 4 Setup of aerodynamic force coefficient measurements.

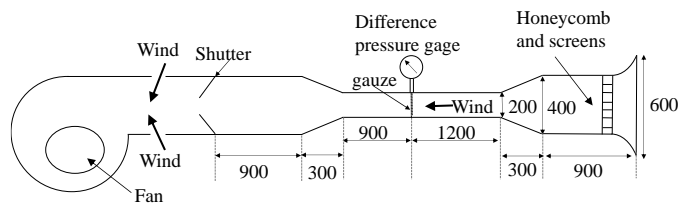


Fig. 5 A schematic of wind tunnel used for measurement of pressure loss coefficients of gauze (unit: mm).

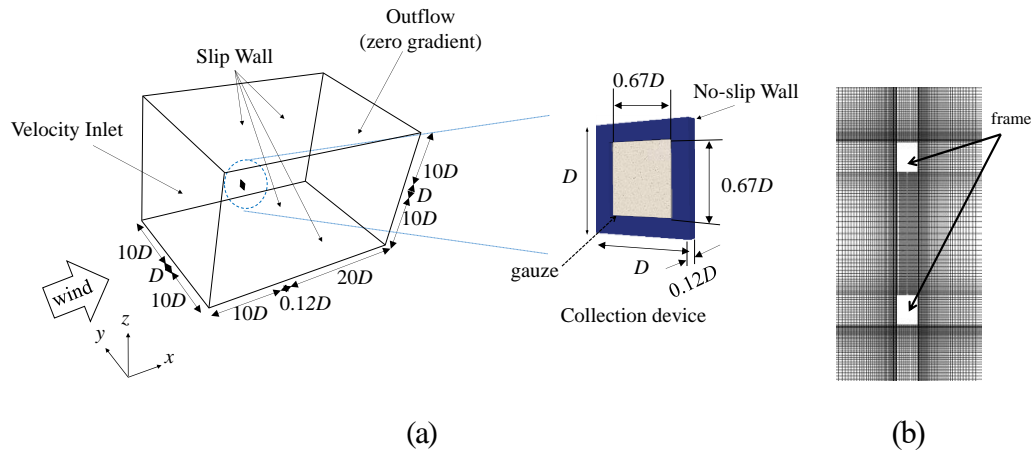


Fig. 6 Calculation domain: (a) whole analysis area and (b) grids near the collection device.

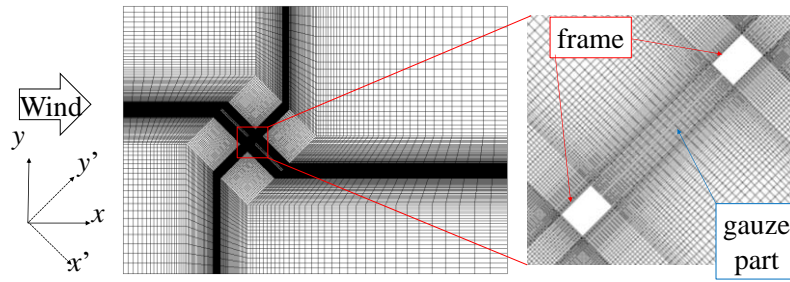


Fig. 7 Calculation grids for the flow field around the collection device with an angle of attack (angle of attack of 45°).

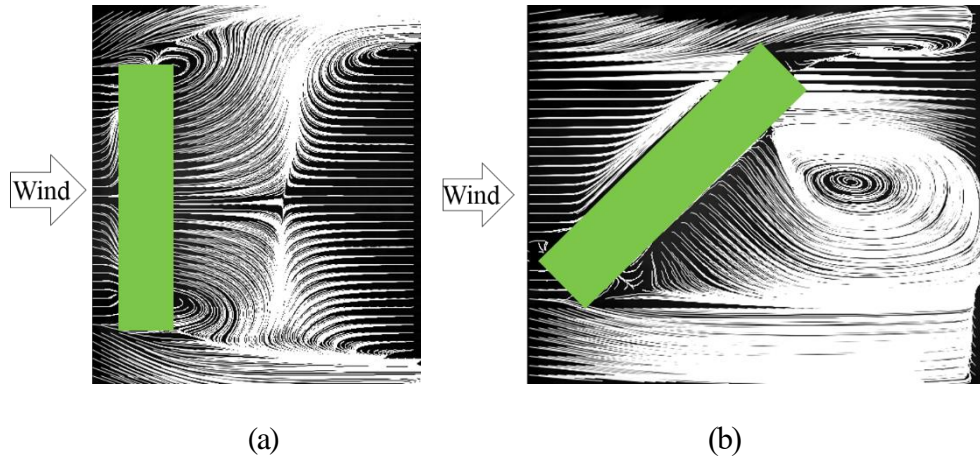


Fig. 8 PIV analysis results of the time-averaged streamline at the center height around the collection device (the wind tunnel velocity is 1 m/s): (a) wind direction 0° , (b) 45°

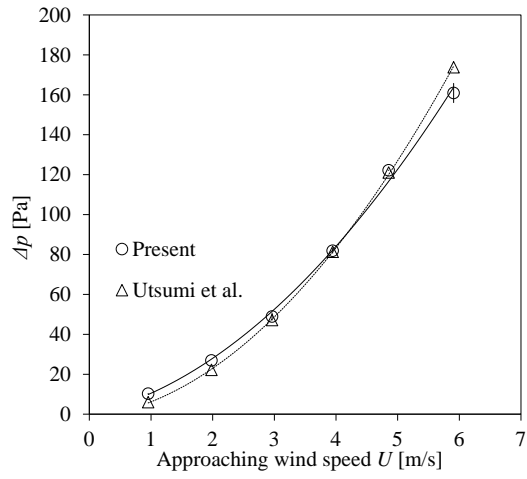


Fig. 9 Comparison of pressure loss values obtained in this experiment with estimated values based on the study by Utsumi et al. [36].

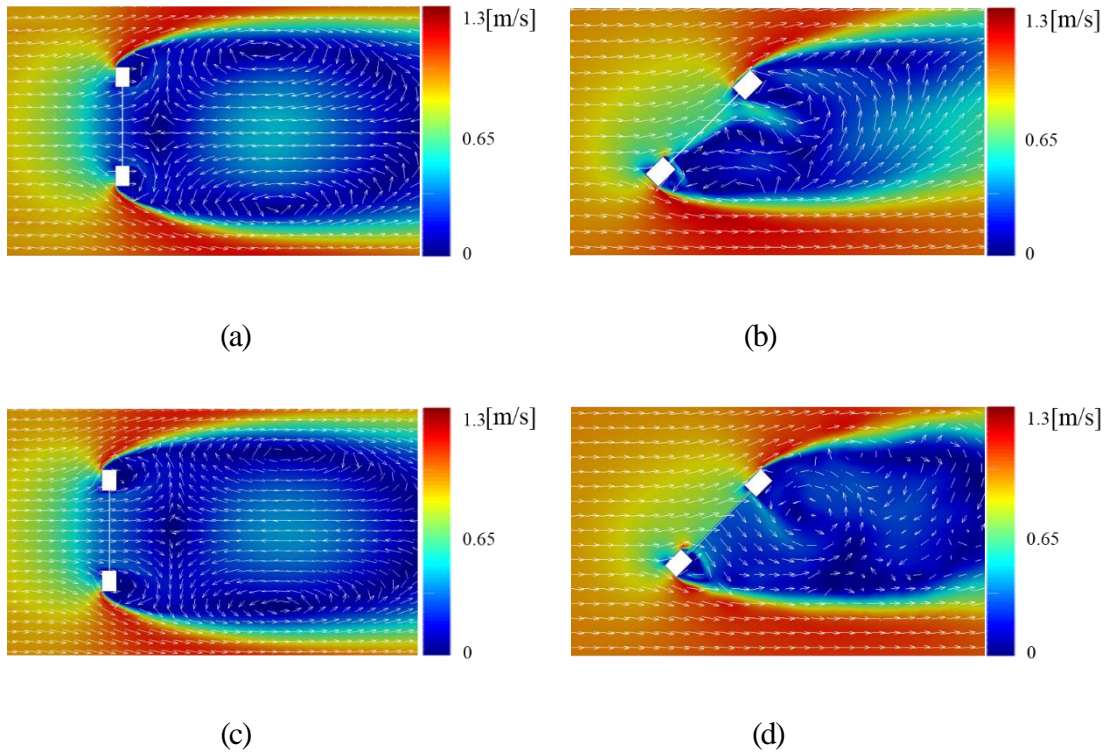


Fig. 10 Time-averaged flow fields at the center height around the collection device for 0° and 45° (wind velocity is 1 m/s): (a)(b) the wind speed by CFD without the tangential resistance of gauze, (c)(d) the wind speed by CFD with the tangential resistance of gauze.

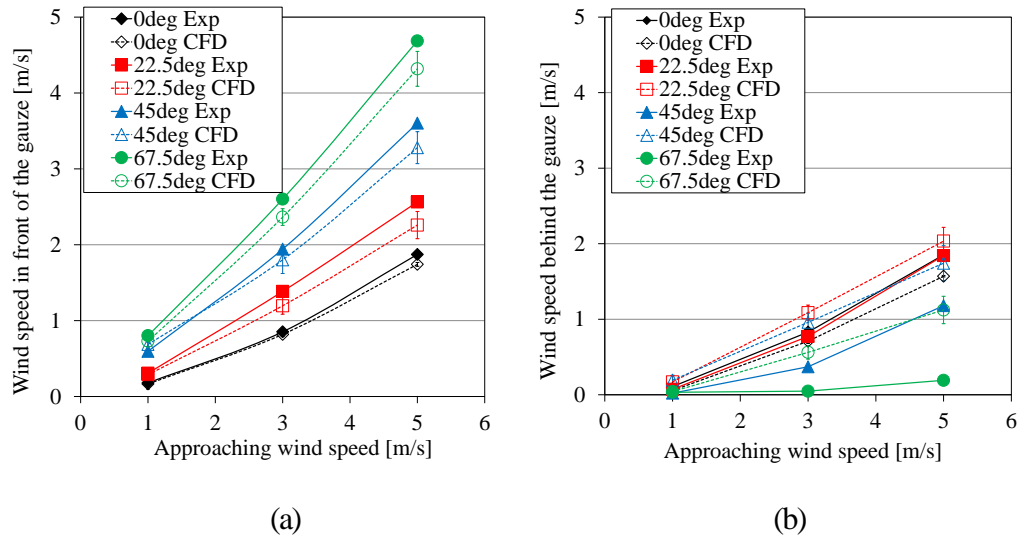


Fig. 11 Comparison of measured and analyzed values of 9-point averaged wind speeds near the gauze without considering the tangential resistance of the gauze: (a) front of the gauze and (b) back of the gauze. The error bars correspond to the standard deviation of the wind speed.

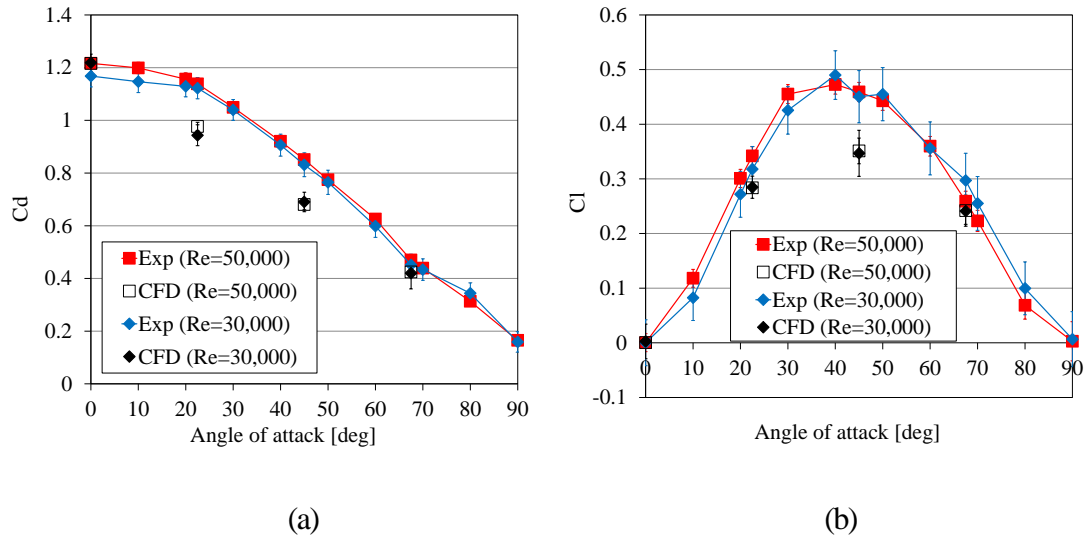


Fig. 12 Comparison of measured and analyzed aerodynamic force coefficients of the collection device without considering the tangential resistance of the gauze: (a) drag force coefficient and (b) lift force coefficient. The error bars correspond to the standard deviation of the aerodynamic force coefficients.

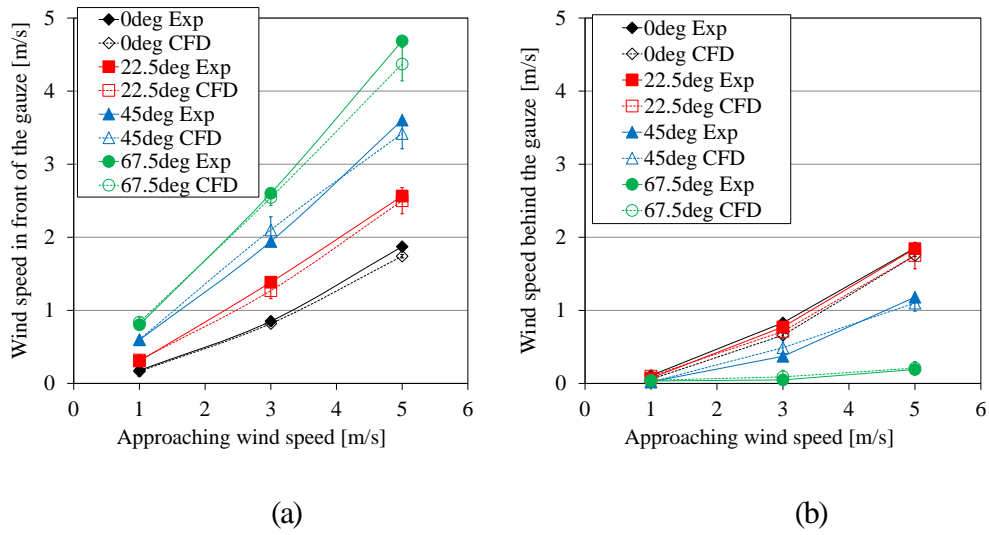
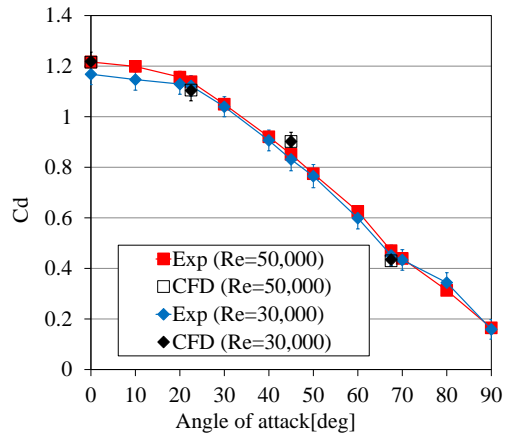
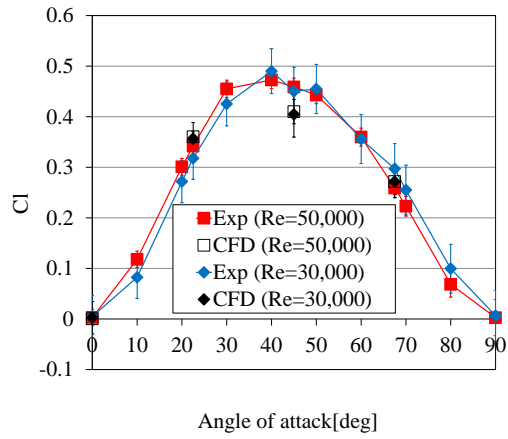


Fig. 13 Comparison of measured and analyzed values of 9-point averaged wind speeds near the gauze when considering the tangential resistance of the gauze: (a) front of the gauze and (b) back of the gauze. The error bars correspond to the standard deviation of the wind speed.



(a)



(b)

Fig. 14 Comparison of measured and analyzed aerodynamic force coefficients of the collection device when considering the tangential resistance of the gauze: (a) drag force coefficient and (b) lift force coefficient. The error bars correspond to the standard deviation of the aerodynamic force coefficients.

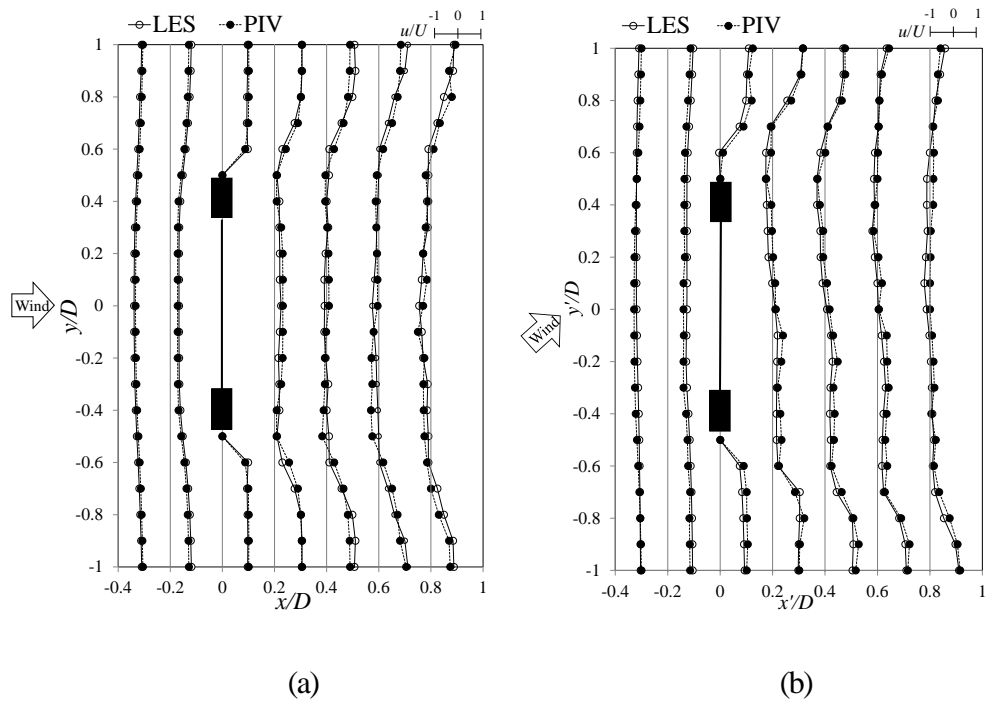


Fig. 15 Comparison of the time-averaged wind speed in the mainstream direction obtained by PIV and LES (approaching wind speed is 1 m/s): (a) Wind direction 0° and (b) 45° . Here, u is the streamwise wind speed, which is made dimensionless by the approaching wind speed U .

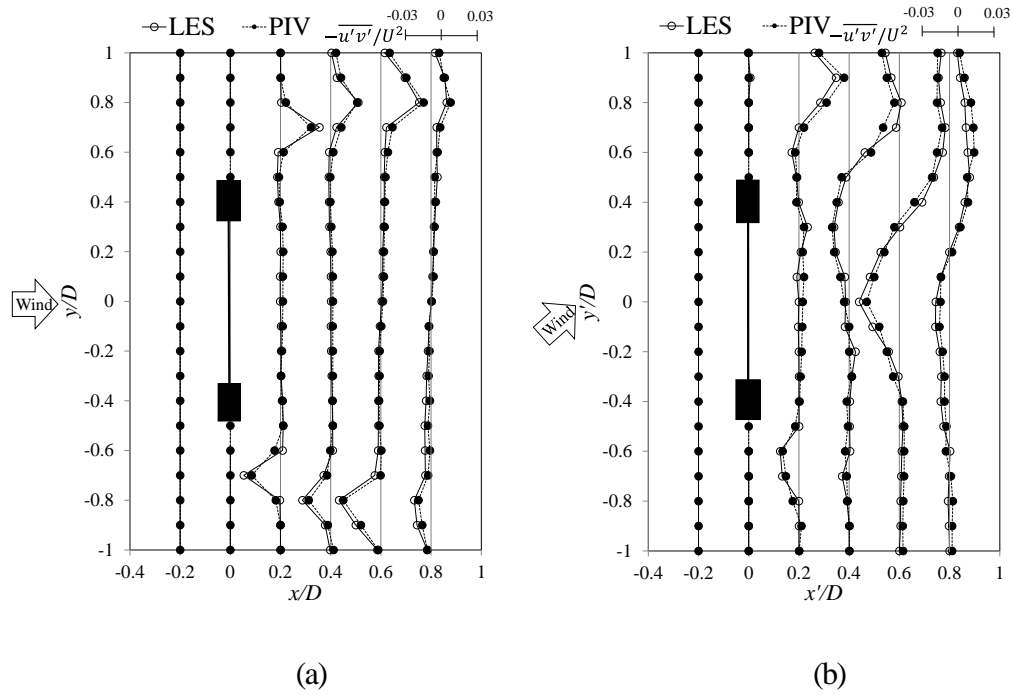
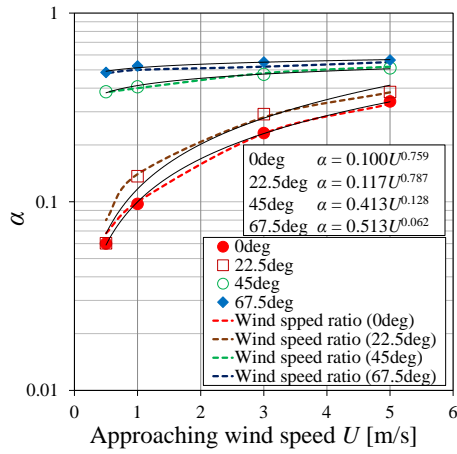
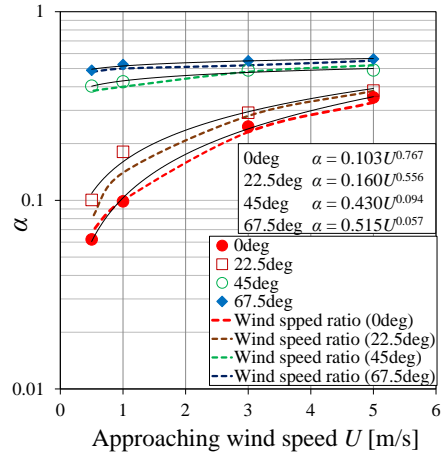


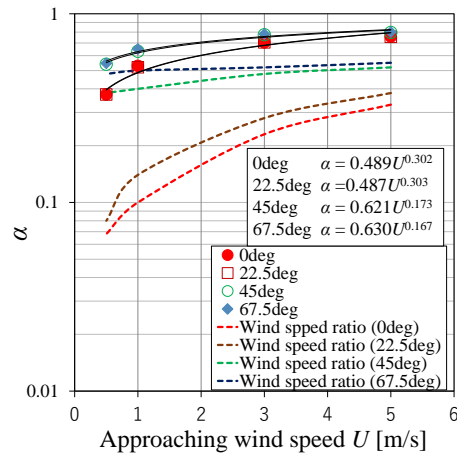
Fig. 16 Comparison of the Reynolds stress ($-\overline{u'v'}/U^2$) obtained by PIV and LES (approaching wind speed is 1 m/s): (a) Wind direction 0° and (b) 45° . Here, u' is the fluctuating streamwise wind speed, and v' is the fluctuating transverse wind speed.



(a)



(b)



(c)

Fig. 17 Analysis results of the arrival rate of particles to the gauze part (α). Particle diameter: (a) $2 \mu\text{m}$, (b) $20 \mu\text{m}$, and (c) $200 \mu\text{m}$. Here, the solid line represents the approximate curve of the arrival rate, and the dotted line represents the wind speed ratio between the approaching wind speed and gauze-surface wind speed.